Characteristics of wall pressure fluctuations in separated and reattaching flows over a backward-facing step:

Part I. Time-mean statistics and cross-spectral analyses

I. Lee, H. J. Sung

Abstract Laboratory measurements were made of wall pressure fluctuations in separated and reattaching flows over a backward-facing step. An array of 32 microphones in the streamwise as well as the spanwise directions was utilized. The statistical properties of pressure fluctuations were scrutinized. Emphasis was placed on the flow inhomogeneity in the streamwise direction. One-point statistics such as the streamwise distribution of rms pressure and autospectra were shown to be generally consistent with the prior results. The peak frequency and the fall-off rate of autospectra demonstrated the shear layer-originated nature of pressure fluctuations. The coherences and wavenumber spectra in the streamwise and spanwise directions were indicative of the presence of dual modes in pressure; one is associated with the large-scale vortical structure in the low-frequency region and the other is the boundary-layer-like decaying mode in the high-frequency region.

List of symbols

AR	aspect ratio of backward-facing step
f	frequency [Hz]
H	step height [m]
j	imaginary unit, $\sqrt{-1}$
k_1	streamwise wavenumber [1/m]
k_3	spanwise wavenumber [1/m]
k_c	convective wavenumber, ω/U_c [1/m]
$R_{pp}(\xi, \zeta, \tau; X_0)$	cross-correlation of pressure with streamwise separation interval ξ, spanwise separation interval ζ and time delay τ at X_0 [Pa^2]
Re$_H$	Reynolds number based on U_0 and H, $U_0 H/v$
Re$_\theta$	Reynolds number based on U_0 and θ, $U_0\theta/v$
U_0	freestream velocity [m/s]
U_c	convection velocity [m/s]
x_R	time mean reattachment length [m]
X_0	streamwise coordinate of reference point [m]
Z_0	spanwise coordinate of reference point [m]

Greek symbols

α_1	decay constant
γ_p	forward flow time fraction
$\Gamma(\xi, \omega; X_0)$	streamwise coherence function of pressure at X_0
$\Gamma(\zeta, \omega; X_0)$	spanwise coherence function of pressure at X_0
θ	boundary layer momentum thickness [m]
v	kinematic viscosity [m^2/s]
ξ	streamwise separation interval [m]
ζ	spanwise separation interval [m]
ρ	density [kg/m^3]
τ	time delay [s]
$\Phi_p(\omega; x, z)$	autospectrum of pressure measured at (x, z) [Pa^2 s]
$\Phi_{pp}(\xi, \omega; X_0)$	streamwise cross spectrum of pressure at X_0 [Pa^2 s]
$\Phi_{pp}(\zeta, \omega; X_0)$	spanwise cross spectrum of pressure at X_0 [Pa^2 s]
$\Phi_{pp}(k_1, \omega; X_0)$	streamwise wavenumber–frequency spectrum of pressure at X_0 [Pa^2 m s]
$\Phi_{pp}(k_3, \omega; X_0)$	spanwise wavenumber–frequency spectrum of pressure at X_0 [Pa^2 m s]
$\varphi(\xi, \omega; X_0)$	phase of cross spectrum [rad]
ω	circular frequency [rad/s]

I. Lee, H. J. Sung
Department of Mechanical Engineering,
Korea Advanced Institute of Science and Technology,
373-1 Kusong-dong Yusong-ku,
Taejon, 305-701, Korea

Correspondence to: H. J. Sung

1
Introduction

Surface pressure fluctuations in turbulent flows, which are a direct measure of the surface excitation force, are closely linked with flow noise generation in the vicinity of the wall (Farabee and Casarella 1986; Lee and Sung 1999). Practical interest in this subject arises because of undesired noise and vibration relevant to turbulent wall flows. To predict structural responses to bounding turbulent flow and consequent flow-induced noise, an accurate measurement of wall pressure fluctuations is required. Much attention has

been given to the accurate measurement of wall pressure fluctuations in the frequency and wavenumber domains. The majority of previous studies have been concentrated on the investigation of spatial and spectral features of wall pressure fluctuations beneath turbulent boundary layers (Schewe 1983; Choi and Moin 1990; Farabee and Casarella 1991).

Typical flow patterns over a backward-facing step at a high Reynolds number display the formation of separated flow as well as the emergence of reattached flow further downstream. The presence of a separated flow, together with a highly energized reattaching flow, gives rise to increased unsteadiness, pressure fluctuations, and structure vibration and noise. A perusal of the relevant literatures reveals that few studies have dealt with the spatio-temporal characteristics of wall pressure fluctuations. A simple analysis of one-point statistics such as rms values or autospectra of the pressure fluctuations has been performed (Mabey 1972; Govinda Ram and Arakeri 1990). One exception is the work by Farabee and Casarella (1986), who measured the coherence function and convection velocity of pressure fluctuations in flows over a backward-facing step. However, due to the limited number and array size of microphones, the large-scale motions were not fully resolved.

Among various statistical properties of the wall pressure fluctuations, the streamwise wavenumber–frequency spectrum is of particular relevance. The wavenumber spectrum provides a useful means to predict the structural response to the excitation of wall pressure fluctuations. To secure the broadband wavenumber characteristics of pressure fluctuations, multiple-arrayed pressure measurements with a streamwise extent of at least several step heights are highly recommended. A literature survey discloses, however, that the multiple-arrayed sensor applications are scarce. This may be attributed to difficulties in practical instrumentation (Lee and Sung 1999).

In the present account, a systematic measurement of wall pressure fluctuations was made in the flow over a backward-facing step. An array of 32 microphones was employed to measure the spatio-temporal statistical features of the fluctuating wall pressure fields. The inhomogeneity of the flow field was analyzed by acquiring the data set with different reference streamwise coordinate X_0. This study aims to provide a comprehensive experimental data set concerning the spatio-temporal statistics of wall pressure fluctuations in flows over a backward-facing step. The values of rms pressure fluctuations as well as frequency spectra were evaluated. The coherence function and wavenumber spectra of pressure fluctuations were also presented. Based on these results, the spatial and spectral characteristics of wall pressure fluctuations were scrutinized. The spatial characteristics in the spanwise direction were also investigated. To see the salient unsteady behavior of pressure fluctuations in the present study, a time-dependent analysis is performed by means of the continuous wavelet transform in Part II. The modulated spatio-temporal behavior of large-scale shed vortices in low frequencies is scrutinized.

2
Experimental apparatus

2.1
Wind tunnel and flow measurement

A subsonic open-circuit wind tunnel, which had been constructed in the earlier work of Chun and Sung (1996), was slightly modified for the present experiment. The settling chamber, honeycomb, and screens were placed in sequence. A smooth contraction fairing with a large contraction ratio (6:1) and flow-conditioning elements (honeycomb and three screens) in the settling chamber ensured high-quality flows in the test section. The dimension of the inlet channel was 630 mm in width, 100 mm in height, and 1000 mm in length. A trip wire was installed at the entrance of the inlet channel to trigger the inlet flow to be fully turbulent. Air was driven by a centrifugal fan and a 5 h.p. motor. The velocity in the test section was controlled by an inverter. The free-stream turbulence intensity was less than 0.6% at speeds 5 to 25 m/s. No significant peaks were found in the spectrum of velocity fluctuations in the main flow. The step edge was attached to the end of the inlet channel, which was 1000 mm downstream of the trip wire. At this location, a constant-area rectangular duct, whose dimension was 630 mm in width, 150 mm in height, and 2500 mm in length, was constructed to act as the backward-facing step. The step height H of the backward-facing step was 50 mm and the aspect ratio $AR = 12.5$. For the present experimental rig, the two-dimensional flow assumption is applicable to a reasonable accuracy, at least for much of the central portion of the test section. An AR ratio greater than 10 has been recommended by Brederode and Bradshaw (1978) to avoid significant side wall effects in the vicinity of the centerline of the channel. Therefore, the flow is assumed to maintain two-dimensionality along the centerline of the test section.

The usual hot-wire technique was used, together with a constant temperature anemometer (TSI-IFA300). A split-film probe (TSI model 1288) was used to measure the fluctuating velocity statistics and the forward-flow time fraction γ_p. The forward-flow time fraction γ_p was defined as the time fraction of downstream flow and was further utilized in estimating the reattachment length x_R (Chun and Sung 1996). A total of 204,800 voltage samples at each position were averaged and sent to a Pentium PC after the velocity signals were digitized by means of a 4-channel A/D converter (UEI WIN-30DS). The A/D converter was equipped with a 12-bit A/D converter through a low-pass filter. All these instruments were remote-controlled using an in-house LabVIEW program. The cut-off frequency for measuring the turbulent properties was fixed at 5 kHz. The forward-flow time fraction was at 100 Hz. A sampling frequency was fixed at 10 and 200 Hz for the above two cases, respectively. The frequency response characteristics of the hot-wire probes were found to be flat below 30 kHz by a square-wave test.

2.2
Pressure fluctuations measurement
In the present study, an Acousticel array microphone system (The Modal Shop, Model TMS130A) was utilized

for sensing the pressure fluctuations. This system consists of 32 electret condenser microphones, with a diameter of 10.54 mm and a height of 25.4 mm, connection cables, and a 32-channel differential amplifier (Model 514A). The sensitivity of each microphone was measured by comparison with a half-inch reference microphone (B & K Type 4133), which was installed together with the Acousticels in an acoustic array calibrator (Model 9080C). A schematic of the calibrator is given in Fig. 1. This calibrator is a rectangular wooden duct, where a standing acoustic wave is developed by a woofer speaker installed in one end. On the other endplate of the calibrator, the reference microphone and the Acousticels were placed. Since the sound field inside the calibrator is a plane wave, the sensitivity as well as the frequency response of each Acousticel can be estimated. The typical sensitivity was about 0.15 V/Pa. The calibration results indicated that the magnitude error and the phase delay were below ± 1 dB and ± 3 degrees, respectively, in the frequency range from 5 to 10 kHz. This "flat" response, together with the wide dynamic range of 42–142 dB, guarantees high levels of measurement accuracy. Here, the reference of decibel scale is 20 µPa. With the knowledge of the sensitivity of each microphone, the fluctuating pressure can be obtained without compensation procedures.

Figure 2 illustrates the installation methods of microphone array in the test section. A 5 mm thick aluminum plate was inserted into a slot machined along the centerline of the section. On each side of the aluminum plate, 1 mm diameter pressure measuring holes and 10.6 mm diameter microphone installation holes were placed concentrically. The Helmholtz resonance frequency from the present apparatus was estimated to be 3750 Hz. As shown in Fig. 2, the interval between each Acousticel $\Delta \xi_0$ was set at 12.5 mm, giving $\Delta \xi_0 / H = 0.25$. Thus, the 32 Acousticel array spans a streamwise extent of $7.75H$. Due to the inhomogeneity of flowfield, the cross correlation of pressure fluctuations $R_{pp}(\xi, \zeta, \tau; X_0) = \overline{p(X_0, Z_0, t)p(X_0 + \xi, Z_0 + \zeta, t + \tau)}$ as well as other cross spectral statistics generally show dependence on X_0. Here, the X_0 reference is the location of the most upstream sensor in the streamwise coordinate, as seen in Fig. 2. In the present study, four values of X_0/H, i.e., 2.0, 4.0, 8.0, and 10.0, were employed.
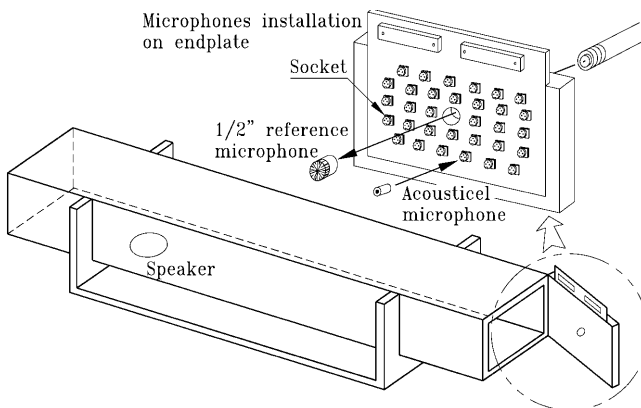

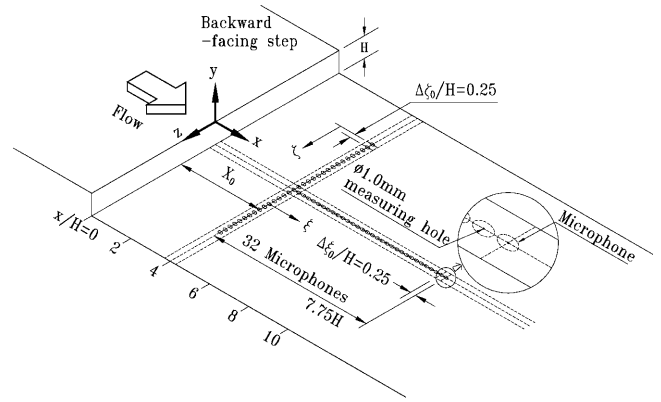**Fig. 1.** Schematic diagram of Acousticel array microphone calibrator

Fig. 2. Schematic diagram of test section

As X_0 is altered, the 32-channel array moves correspondingly in the streamwise direction. For each measurement with different X_0, 32 pressure–time histories were acquired with the sampling frequency of 7812.5 Hz using an A/D converter DT2839 (Data Translation). This sampling frequency was selected with a view toward minimizing the aliasing of Helmholtz resonance from the microphone hole. To reduce the interchannel sampling delay, one of every four pressure readings was recorded, which gave an effective sampling frequency of 1953.125 Hz. This undersampling was performed when the cross-spectrum was measured. Each pressure–time history contained 409,600 points of data, and they were stored in a Pentium personal computer. To estimate the auto- and cross-spectra, 400 ensemble sets containing 2048 data points were used with the overlapped processing technique in Bendat and Piersol (1991). The random error ε_r was estimated, $\varepsilon_r = 1/\sqrt{n_d}$, where n_d is the number of ensemble sets (Bendat and Piersol 1991). The corresponding random error amounts to 5%. Along with this streamwise array, the spanwise arrays, located at $X_0/H = 2.0, 4.0, 8.0$, and 10.0, were utilized to examine the spatial characteristics in the spanwise direction.

3
Experimental results

3.1
The flow parameters
In the present experiment, the Reynolds number based on the step height $Re_H = 33000$ is selected, which is the same as in the experiment of Chun and Sung (1996). When rescaled by using the momentum thickness, this corresponds to $Re_\theta = 1300$. Among the various data representing the backward-facing step flow, the reattachment length x_R is frequently used as a representative quantity in a time-mean sense. In order to find the reattachment length, the forward-flow time fraction γ_p in the vicinity of the wall ($y/H = -0.98$) is measured by using a split film probe (TSI model 1288). The time-mean reattachment position x_R can be defined as the point where the forward-flow time fraction has the value $\gamma_p = 0.5$. The reattachment length is found to be $x_R = 7.4\,H$. Details regarding the mean and fluctuating velocity profiles and other quantities can be found in Chun and Sung (1996).

3.2
One-point statistics of pressure fluctuations

In Fig. 3, streamwise distributions of the rms pressure fluctuations normalized by the inflow dynamic pressure $(1/2\rho U_0^2)$ are compared with the data of Driver et al. (1987), Farabee and Casarella (1986), and Le and Moin (1994). The mean pressure coefficient C_p from Chun and Sung (1996) is also displayed for comparison. The normalization of abscissa by using the reattachment length is adopted here to compensate for different flow conditions (Mabey 1972). It is seen that the maximum energy of pressure fluctuations occurs slightly upstream of x_R. This is a well-documented feature of separated and reattaching flows. (Mabey 1972; Kiya and Sasaki 1983; Cherry et al. 1984). The rms values begin to rise rapidly at about $x/x_R = 0.5$. The mean pressure coefficient C_p also begins to increase at this location. Note that the increased level of rms value is closely correlated with the mean pressure recovery (Govinda Ram and Arakeri 1990). Devenport and Sutton (1991) identified the large-scale velocity fluctuations in the near-wall region, which are driven by the pressure gradient fluctuations imposed by the separated shear layer. This suggests that the pressure fluctuations are mainly generated by unsteadiness imposed by the shear layer, rather than the near-wall behavior bounded in the recirculation zone. After reattachment, the rms value decreases slowly. This is attributed to the lack of free shear layer activity. Furthermore, the slow reduction implies that the large-scale vortical motion after reattachment persists, as indicated by Farabee and Casarella (1986).

The probability density functions (PDFs) of pressure fluctuations at various streamwise locations are plotted in Fig. 4, together with a Gaussian density. The measured density is almost the same as the Gaussian density. Note that Schewe (1983) reported a deviation of the pressure PDF from the Gaussian PDF in a turbulent boundary layer. Schewe showed that as the diameter of pressure sensor decreases, the deviation of the measured probability density from the Gaussian density increases and attributed this to the central limit theorem of random variables. In the light of this phenomenon, it might be argued that the near-Gaussian probabilistic character is due to inadequa-
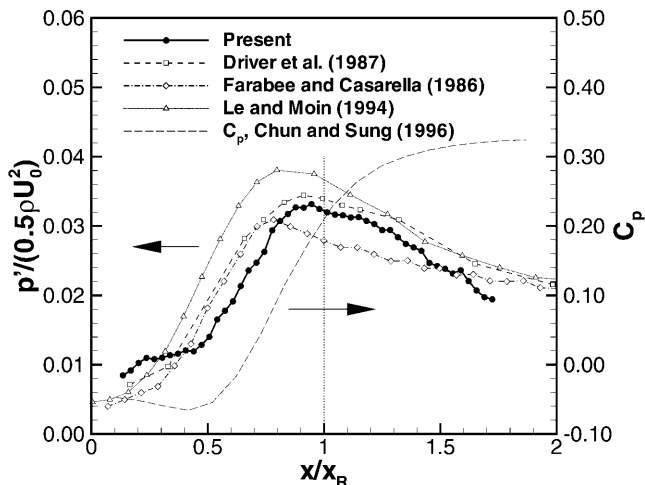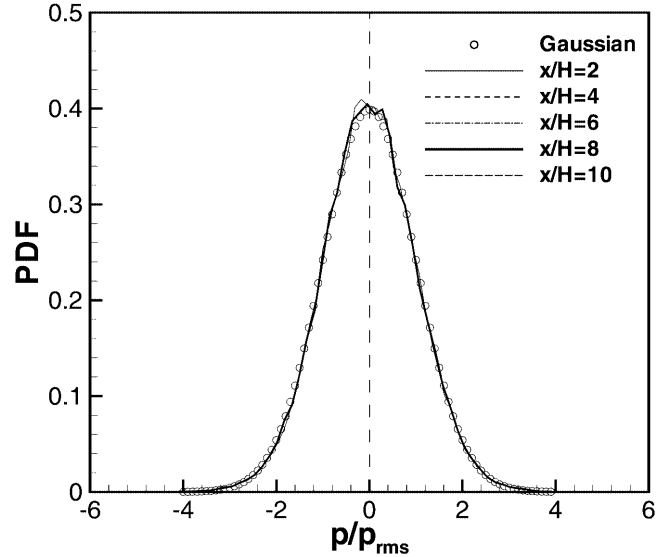

Fig. 4. Probability density functions of pressure at various streamwise locations

cies of the apparatus in resolving the high-wavenumber components of pressure fluctuations. However, the dominant influence of large-scale vortical structures on pressure fluctuations in this flow regime indicates that the most relevant scales of pressure-generating eddies are the integral scales, not the wall unit as in a turbulent boundary layer. It is well known that the near-wall reverse flow is not an active source of turbulence energy (Adams and Johnston 1988; Devenport and Sutton 1991; Le and Moin 1994). Hence, the attenuation of high-wavenumber components is negligible, since the present apparatus has sufficient resolution to delineate the large-scale vortices. Although the present PDF is not fully resolved with vanishingly small pressure transducers, the near-Gaussian probability is a typical character of the pressure fields rather than the degraded statistics due to bad spatial resolution of the sensor.

The pressure autospectra measured at various locations are displayed in Fig. 5. At $x/H = 2$, compared with other locations, the spectrum level is generally low except at very low frequencies ($fH/U_0 \sim 0.015$). When rescaled with the reattachment length x_R, as Mabey (1972) proposed, the afore-mentioned nondimensional frequency $fx_R/U_0 \sim 0.11$ coincides with the frequency of the flapping motion, i.e., very low frequency unsteadiness which indicates a growth–decay cycle of the whole separation bubble (Eaton 1980; Cherry et al. 1984). Cherry et al. (1984) also indicated the relative dominance of very low frequency components in this region close to the separation point. For all the locations, the pressure spectrum reaches a maximum at $fH/U_0 \sim 0.068$, which is nearly the same as $fH/U_0 \sim 0.066$ in Eaton (1980). Also, the frequency $fx_R/U_0 \sim 0.50$ falls within the maximum frequency range $0.5 \leq fx_R/U_0 \leq 0.80$ of Mabey (1972) and is comparable to the frequency of large-scale vortical structure, i.e., $fx_R/U_0 \sim 0.60$ (Driver et al. 1987). In addition, as x/H increases, the high-frequency components continue to increase. The fall-off rate approaches asymptotically the $-7/3$ power. George et al. (1984) developed a spectral
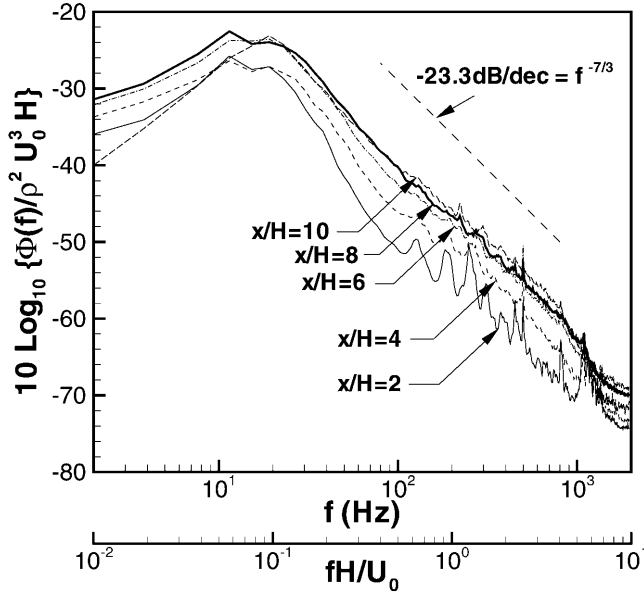

Fig. 3. Streamwise distributions of rms pressure

Fig. 5. Autospectra of pressure at various streamwise locations

model for turbulent pressure fluctuations by Fourier – transforming the solution of Poisson equation for a free shear flow with constant mean shear. They demonstrated the $-11/3$ and $-7/3$ fall-off rates for the mean shear-turbulence interaction term and the turbulence-turbulence interaction term, respectively. The steeper slope of the spectra in the former part of recirculation region ($2.0 \leq x/H \leq 4.0$) for $0.1 \leq fH/U_0 \leq 0.5$ exhibits the influence of the mean shear-turbulence interaction, even though the spectra show a number of peaks in high frequencies, e.g., $fH/U_0 \geq 0.5$. These peaks might be attributed to the tunnel noise from the fan. Further downstream of this location ($x/H \geq 6.0$), the turbulence-turbulence interaction term becomes more prominent due to the enhanced small scale activity, which collaborates convergence of the fall-off rate toward the $-7/3$ power. These observations provide some conclusion that the pressure fluctuations are largely attributable to the free shear layer model, even after reattachment. Note that the slow relaxation is suggested by Farabee and Casarella (1986), who addressed the deviation of pressure spectra from the equilibrium boundary layer state as far as 72 step heights downstream of the step. Furthermore, the close resemblance of spectra after reattachment is supported by this slow relaxation process. In summary, a relative importance of the shear-layer-originated spatio-temporal characteristics over the boundary-layer-like features is confirmed in the spectra.

3.3
Spatial characteristics of pressure fluctuations in the streamwise direction
The spatial characteristics of the pressure fluctuations are obtained from the cross spectrum $\Phi_{pp}(\xi, \omega; X_0)$, which is defined between two locations separated by ξ as

$$\Phi_{pp}(\xi, \omega; X_0) = \int_{-\infty}^{\infty} R_{pp}(\xi, 0, \tau; X_0) e^{-j\omega\tau} \, d\tau \ , \qquad (1)$$

in which $R_{pp}(\xi, 0, \tau; X_0)$ represents the cross correlation of wall pressure fluctuations. Again, the dependence on the reference point X_0 is considered from the flow inhomogeneity. A normalized magnitude of the cross spectrum is employed here to quantify the change in the pressure field over the distance ξ. This function, termed the coherence $\Gamma(\xi, \omega; X_0)$, is defined as

$$\Gamma(\xi, \omega; X_0) = \frac{|\Phi_{pp}(\xi, \omega; X_0)|}{[\Phi_p(\omega; X_0, Z_0)\Phi_p(\omega; X_0 + \xi, Z_0)]^{1/2}} \ . \qquad (2)$$

Note that the coherence defined above is the square root of the ordinary coherence function $\Gamma^2(\xi, \omega; X_0)$ (Bendat and Piersol 1991). Two-dimensional contour plots of the coherence with $X_0/H = 2.0$ and $X_0/H = 8.0$ are presented in Fig. 6a and b, respectively. An inspection of Fig. 6 reveals that the coherence attains local maxima at particular locations away from the zero axis. As seen in Fig. 6, these maxima can be connected by straight lines to exemplify the definite "ridges" in the frequency-scale space. The separation interval (ξ) along the ridge, i.e., the "wavelength" of the corresponding eddies, decreases with increasing frequency. Considering the regular distribution of large-scale vortices, these definite "ridges" are attributable to the high degree of correlation between two adjacent large-scale vortices. Kiya and Sasaki (1985) demonstrated that, between large-scale vortices, there exists a "pseudo-vortex", which is actually a secondary motion induced by the entrainment. This "pseudo-vortex" is different from the conventional large-scale vortex in the sense that it is not associated with the highly turbulent regions. Since these two structures are of dissimilar nature, the accompanying small scale components would show different
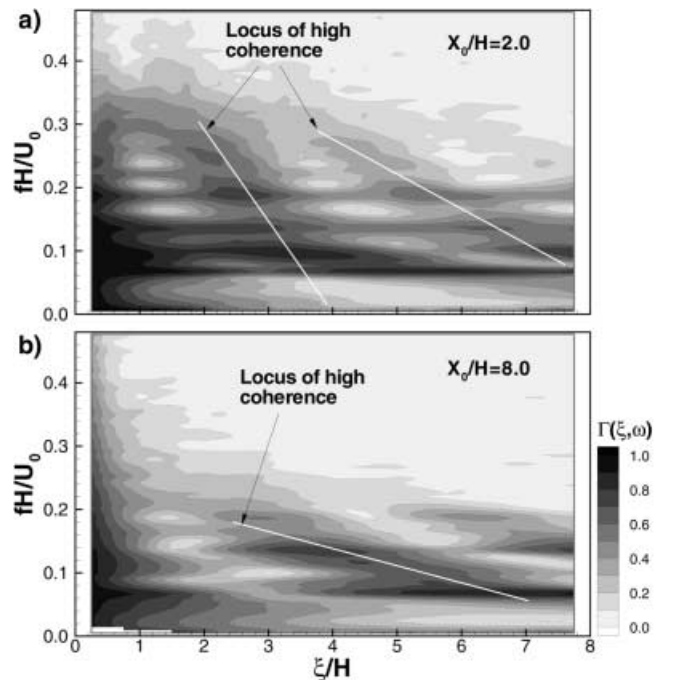

Fig. 6a, b. Contour plots of streamwise coherence at **a** $X_0/H = 2.0$; **b** $X_0/H = 8.0$

degrees of correlation according to their "parent" structures. For example, the center region of the pseudo-vortex is not correlated with the large-scale vortices, and vice versa. Detailed investigations of these two structures, which would essentially require conditional samplings of flow field, are beyond the scope of the present study. The above reasoning provides a qualitative basis for the alternating presence of the "ridges" and "troughs" of coherence in the (ξ, ω) space. Extended explanations of the frequency characteristics will be made in connection with the evaluation of the similarity variable $\omega\xi/U_c$ in Figs. 7–10.

In Fig. 6, the lowest frequency with the peaks is $fH/U_0 \sim 0.068$, i.e., the aforementioned frequency of large-scale vortical structures. For $X_0/H = 2.0$, the peaks and valleys of the coherence are found in the frequency range up to $fH/U_0 \sim 0.3$, while this range is reduced to $fH/U_0 \le 0.20$ for $X_0/H = 8.0$. In addition, for $X_0/H = 8.0$, the scale extent of the ridge is enlarged, compared with that for $X_0/H = 2.0$. The cross spectrum $\Phi_{pp}(\xi, \omega; X_0)$ is evaluated from a statistical average between the reference point X_0 and a certain downstream point $X_0 + \xi$. This can be considered as a frequency as well as a scale filter for the correlated modes at the reference point. In this context, the above behavior of the coherence depicts a situation where the decrease of frequency content and the increase of scale take place along the streamwise coordinate. This observation is consistent with the transverse spreading of the shear layer along the streamwise direction, which is caused by the entrainment of fluid from both sides of the separated shear layer. Thus, the large-scale vortex grows up until it reattaches the wall, and the growth rate has been found to be approximately linear (Eaton 1980).

In the coherence measurement of Farabee and Casarella (1986), the sensor separation was limited to small values of $\xi/H = 1.0$ and $\xi/H = 1.5$. The coherence in the recirculation region ($X/H = 2, 4$ and 6) attained a local maximum at $\omega\xi/U_c \sim 3.0$. However, their analysis was focused on the high-frequency decay characteristics. The existence of maximum frequency modes was not considered. A comparison of the decay rates measured at various positions indicated that the reattaching flow ($X/H = 8.0$) was the least-organized of all locations, which is contrary to the present results. This discrepancy is attributable partly to the limitations of their data, and partly to the unrealistic basis of boundary-layer-decaying model, such as the Corcos model. In the Corcos model, only a uniform decay from a "main lobe" along either the zero frequency axis $\omega = 0$ or the zero separation axis $\xi = 0$ was predicted in terms of a similarity variable of $\omega\xi/U_c$. In the present study, however, the main lobe of the coherence at reattachment has moved to far larger scales, not decayed out. Accordingly, the pressure as well as the flowfield are highly organized, which is consistent with other studies (Eaton and Johnston 1981; Kiya and Sasaki 1983).

In order to assess the effectiveness of the similarity variable $\omega\xi/U_c$, the coherences with respect to frequency and separation interval are plotted separately in Figs. 7–10. In the Corcos model, the coherence is expected to decay exponentially with $\omega\xi/U_c$;

$$\Gamma(\xi, \omega) = \exp(-\alpha_1 |\omega\xi/U_c|) \ , \tag{3}$$

where α_1 is an empirically determined decay constant. In this model, the X_0 dependence is not incorporated. Figures 7 and 8 illustrate the coherence with fixed separation ξ_0 for $X_0/H = 4.0$ and $X_0/H = 10.0$. The independent variables
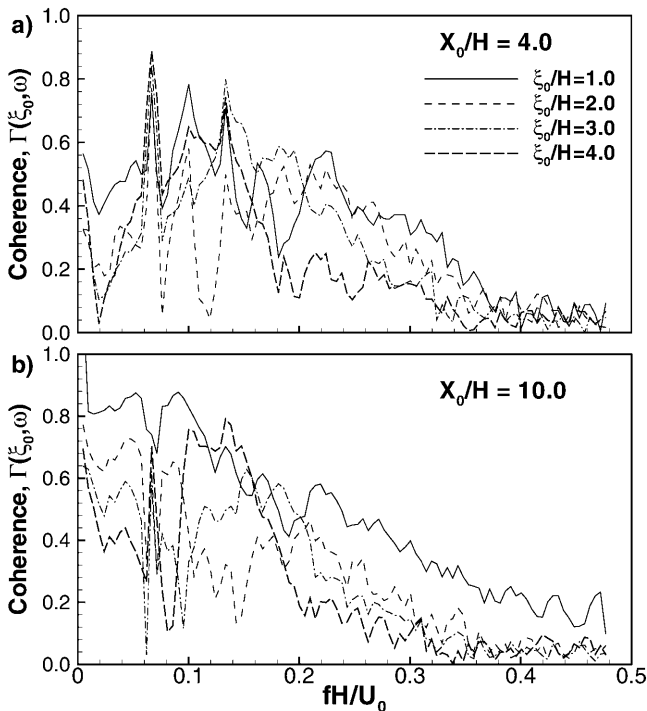
Fig. 7a, b. Streamwise coherence as a function of fH/U_0 at **a** $X_0/H = 4.0$; **b** $X_0/H = 10.0$
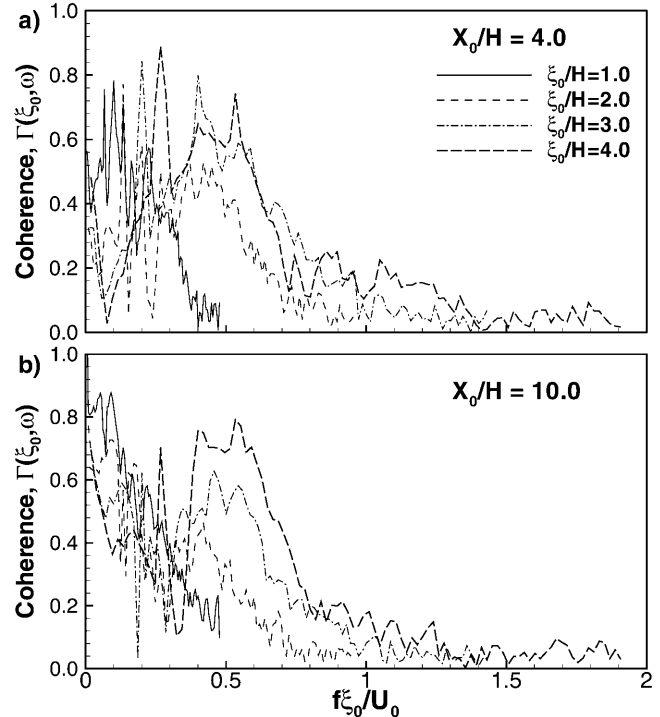

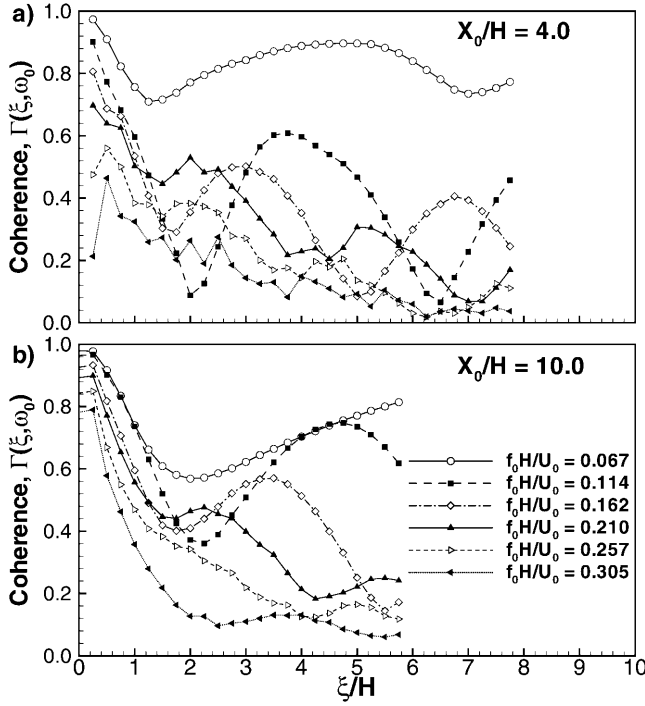**Fig. 8a, b.** Streamwise coherence as a function of $f\xi_0/U_0$ at **a** $X_0/H = 4.0$; **b** $X_0/H = 10.0$

Fig. 9a, b. Streamwise coherence as a function of ξ/H at **a** $X_0/H = 4.0$; **b** $X_0/H = 10.0$
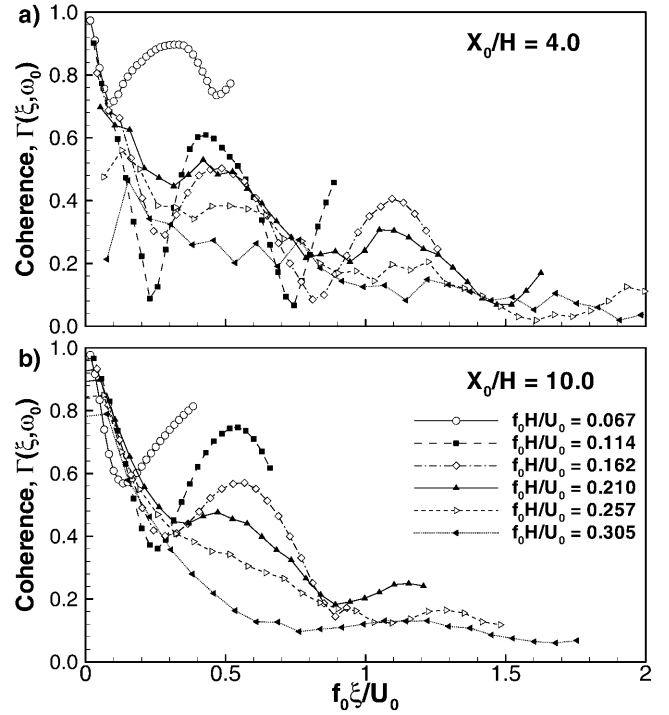

Fig. 10a, b. Streamwise coherence as a function of $f_0\xi/U_0$ at **a** $X_0/H = 4.0$; **b** $X_0/H = 10.0$

are fH/U_0 in Fig. 7 and $f\xi_0/U_0$ in Fig. 8, respectively. Note that the normalization with the convection velocity has not been attempted. This is because the convection velocities become singular in many cases. An appropriate frequency scale should be selected to represent the coherence data with different values of ξ_0. One is fH/U_0, which is the absolute frequency scale. The other is $f\xi_0/U_0$, which is in proportion to the "phase" of the cross spectrum $f\xi_0/U_c$ ($U_c \simeq 0.6U_0$). An examination of these two scales in Figs. 7 and 8 reveals that fH/U_0 gives a better collapse between the peaks from large-scale vortical structure around $fH/U_0 \sim 0.068$. On the contrary, $f\xi_0/U_0$ is more effective in higher frequencies $f\xi_0/U_0 \geq 0.4$.

The coherences with respect to ξ at four fixed frequencies f_0 are shown in Figs. 9 and 10. The coherence at the frequency of large-scale vortices ($f_0H/U_0 = 0.067$) is far higher than those from other frequencies. For other high-frequency components, the scaling with $f_0\xi/U_0$ in Fig. 10 shows a better collapse between the peak locations than the scaling with ξ/H in Fig. 9. The peak frequency itself varies from $f_0\xi/U_0 \sim 0.45$ at $X_0/H = 4.0$ to $f_0\xi/U_0 \sim 0.60$ at $X_0/H = 10.0$. Note that increasing the frequency over $f_0H/U_0 \sim 0.25$ yields a monotonic decay of the coherence (Fig. 6).

The better collapse of the oscillatory behavior of coherence in Figs. 8 and 10 implies that an alternative similarity model other than the Corcos model can be established on the basis of some definite length scale. In general, the solution of Poisson equation for pressure fluctuations is given by the convolution of the source terms with a Green's function. The pressure fluctuations at one point are thus affected by the velocity fluctuations in the whole flow field. In a turbulent boundary layer, the

quasi-streamwise vortices have been regarded to play an important role in generating wall pressure fluctuations (Dhanak et al. 1997; Chang et al. 1999). While the individual streamwise vortex has a specific dimension, the resulting pressure field depends on the similarity variable $\omega\xi/U_c$, rather than on the specific scale. This contradicting result could be explained in terms of a spatial average of the contributions from numerous streamwise vortices in the whole flow field. Furthermore, the dimension of each vortex is very small compared to typical dimensions of flow field. The turbulent boundary layer behaves as a "continuous source" and the scale information of individual source is effectively "forgotten" by the wall pressure field.

On the contrary, in the separated and reattaching flow, the main contribution comes from the large-scale vortical structures, whose dimension is comparable to the flow field dimensions. Hence, the pressure field is governed by this "monochromatic source" with definite wavenumber composition. Note that the collapse of coherence peaks holds for $0.1 \leq fH/U_0 \leq 0.25$. Below this frequency band, i.e., at the frequency of the large-scale vortices, the coherence is high over very long distances. On the other hand, for $fH/U_0 > 0.25$, the decaying character of coherence prevails with respect to the similarity variable. Consequently, the frequency band $0.1 \leq fH/U_0 \leq 0.25$ is regarded as a "buffer range", where a transition from coherent mode to decaying mode emerges. In summary, the spatial character of pressure fluctuations is classified into the coherent mode from large-scale vortices and the decaying mode in high frequencies.

From the phase of cross spectrum $\varphi(\xi, \omega; X_0)$, the convection velocity $U_c(\xi, \omega; X_0)$ is defined as,

$$U_c(\xi, \omega; X_0) = -\omega \xi / \varphi(\xi, \omega; X_0) \ . \tag{4}$$

This definition is based on the Corcos model, where the cross spectral density is given as
$\Phi_{pp}(\xi, \omega) = \Phi_p(\omega) \exp(-\alpha_1 |\omega \xi / U_c|) \exp(-j|\omega \xi / U_c|)$.
Thus, the magnitude and phase of the cross spectrum describe the decay and convection of pressure field, respectively.

Figure 11 represents the convection velocity normalized by the freestream velocity. Care has been exercised in the estimation of the phase $\varphi(\xi, \omega; X_0)$ by utilizing an appropriate phase unwrapping algorithm, thereby ensuring the continuous phase without 2π-jumps. In Fig. 11, the convection velocity is crowded with many singularities at low frequencies, but approaches approximately $0.6U_0$ in high frequencies. Furthermore, the separation intervals $\xi_0/H = 4.0$ at $X_0/H = 4.0$ and $\xi_0/H = 3.0$ at $X_0/H = 10.0$ yield unrealistically high convection velocities, irrespective of frequency. In addition, the singular region of convection velocity in the (ξ, ω) space (not shown here) overlaps the low-coherence troughs in the corresponding plots of coherence. The "singular scale" of $\xi_0/H = 4.0$ at $X_0/H = 4.0$ corresponds to the secondary trough between the high coherence ridges, whereas the scale of $\xi_0/H = 3.0$ at $X_0/H = 10.0$ corresponds to the primary trough between the $\xi/H = 0$ axis and the ridge. Taking into account of the above-stated model of "pseudo-vortex" between two large-scale vortices, the singularity behavior seems to be caused by a "phase disruption" between two locations with little correlation. In the case of primary trough (Fig. 11b), the singular scale $\xi_0/H = 3.0$ represents half of the average distance between two large-scale vortices of $0.77x_R$, which is consistent with $0.75x_R$ in Kiya and Sasaki (1983). In other sense, the singular region may be related to a shear

layer flapping motion that would produce a very high trace wave speed in the streamwise direction.

Another eminent feature of the convection velocity is its positive definiteness even in the recirculation region. A literature survey indicates that the sign of convection velocity in the recirculation region is controversial; Heenan and Morrison (1998) found a negative convection as well as a positive convection from the cross correlation $R_{pp}(\xi, \tau)$, particularly in the recirculation region close to the step. On the contrary, Farabee and Casarella (1986) found no evidence of negative convection. The present result is in favor of the result of Farabee and Casarella. However, an intermittent recession of peak in the cross-correlation $R_{pp}(\xi, \zeta, \tau; X_0)$ is observed in the present study, which is similar to the finding of Heenan and Morrison. This intermittent unsteady character is mainly correlated with large-scale vortical structures. The singularities and ambiguities in the convection velocity reflect the drawbacks of the Corcos model. The dominance of the positive value is again consistent with the above-mentioned concept of overriding-shear layer-generated pressure.

A more instructive view of the convective feature is provided from the streamwise wavenumber–frequency spectrum $\Phi_{pp}(k_1, \omega; X_0)$, which is obtained by Fourier transforming the streamwise cross spectrum $\Phi_{pp}(\xi, \omega; X_0)$ with respect to ξ. The wavenumber spectrum obtained in boundary layer flows shows a very distinctive convective ridge (see, for example, Fig. 7 of Panton and Robert 1984). In Figs. 12 and 13, where the wavenumber spectra at four locations are depicted, the convective ridges are also found. The black solid line with the inclination of $0.5/0.3 = 0.6^{-1}$ indicates a constant convection velocity of $U_c/U_0 \equiv (f/k_c)/U_0 = (fH/U_0)/(k_cH) = 0.3/0.5 = 0.6$. As the flow goes downstream, the frequency content of the
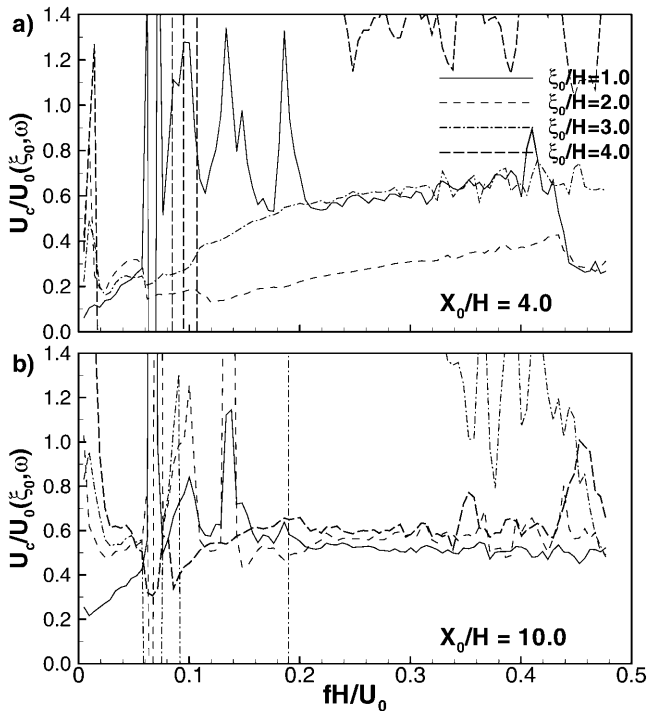
Fig. 11a, b. Convection velocity as a function of fH/U_0 at **a** $X_0/H = 4.0$; **b** $X_0/H = 10.0$
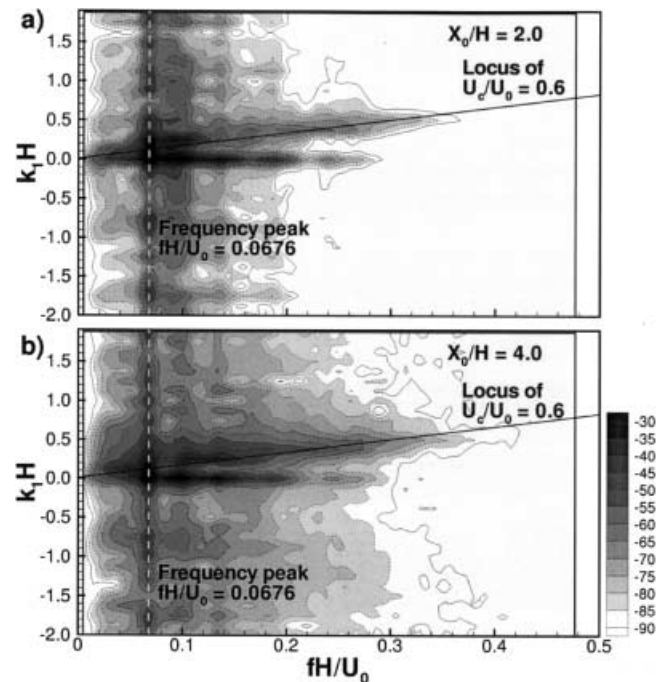

Fig. 12a, b. Streamwise wavenumber–frequency spectra at **a** $X_0/H = 2.0$; **b** $X_0/H = 4.0$

convective ridge is enlarged up to high frequencies. At $X_0/H = 8.0$ (Fig. 13a), the gradient of the ridge in the k_1-direction is the smallest and it increases at $X_0/H = 10.0$ (Fig. 13b). The local minima of the gradient at $X_0/H = 8.0$ represent a dispersion of scales from the interaction between the shear layer and the wall during reattachment. Up to $X_0/H = 10.0$, the convective ridge becomes narrower, which exemplifies more regular scale composition. Since it is well known that the coherent vortical structure is sustained over fairly long distances after reattachment (Farabee and Casarella 1986; Le and Moin 1994), this process suggests that a certain selective action in favor of the specific length scale, i.e., the scale of large-scale vortices, may arise to generate a more pronounced convective ridge.

There exist a couple of notable features found in the wavenumber spectra. At first, in all cases, the wavenumber spectra gain a local maximum at a particular frequency, dispersed in all wavenumbers. This maximum frequency, marked by a white dashed line, is identical to the frequency of large-scale vortical structure. It is noteworthy that the maximum frequency has been shifted towards $fH/U_0 = 0.0954$ at $X_0/H = 10.0$ (Fig. 13b), which is in support of the reduction of vortical scale after reattachment. Second, a stationary mode along the $k_1 = 0$ axis can be observed particularly in the recirculation region (Fig. 12). The presence of the zero wavenumber mode might be attributed to the tunnel acoustics mode, which indeed attains a near-zero maximum wavenumber $k_1 = \omega/c_0$ in flows of low Mach number (c_0 is the speed of sound). However, this acoustic mode can be discounted, because the corresponding frequencies are too low and broad. Note that the noise component can be found for $fH/U_0 \geq 0.5$, beyond the frequency range under consid-
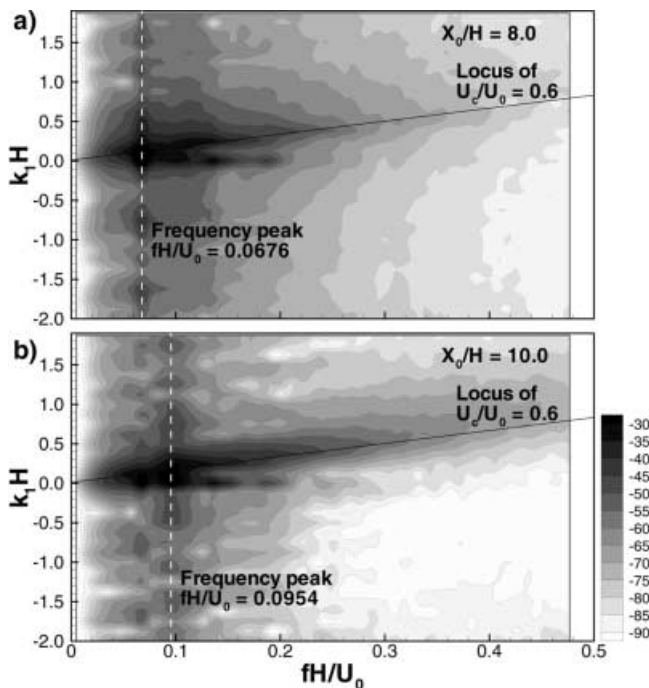

Fig. 13a, b. Streamwise wavenumber–frequency spectra at **a** $X_0/H = 8.0$; **b** $X_0/H = 10.0$

eration. The mechanism underlying these features is associated with the flapping motion, in which the separation bubble undergoes a global, periodic enlargement and shrinkage. The flapping motion does not convect downstream and is found to be more dominant in the recirculation region close to the step (Cherry et al. 1984). At $X_0/H = 2.0$ in Fig. 12a, the stationary mode is nearly comparable to the convective ridge, and becomes less pronounced as the flow goes downstream. According to the visualization study by Cherry et al. (1984), intensive and quiescent states of vortex shedding are shown to alternate each other after the phase of flapping motion. In other words, this observation suggests a modulation of vortical structure by the flapping, thereby giving rise to variations in the orderly structure of large-scale vortices.

3.4
Spatial characteristics of pressure fluctuations in the spanwise direction

A similar analysis on the spatial characteristics in the spanwise direction is extended from the spanwise cross spectrum $\Phi_{pp}(\zeta, \omega; X_0)$, the spanwise coherence $\Gamma(\zeta, \omega; X_0)$, and the spanwise wavenumber–frequency spectrum $\Phi_{pp}(k_3, \omega; X_0)$, defined as follows;

$$\Phi_{pp}(\zeta, \omega; X_0)$$

$$= \int_{-\infty}^{\infty} R_{pp}(0, \zeta, \tau; X_0) e^{-j\omega\tau}\, d\tau$$

$$= \int_{-\infty}^{\infty} \overline{p(X_0, Z_0, t)p(X_0, Z_0 + \zeta, t + \tau)}\, e^{-j\omega\tau}\, d\tau \quad , \quad (5)$$

$$\Gamma(\zeta, \omega; X_0) = \frac{|\Phi_{pp}(\zeta, \omega; X_0)|}{[\Phi_p(\omega; X_0, Z_0)\Phi_p(\omega; X_0, Z_0 + \zeta)]^{1/2}} \quad , \quad (6)$$

$$\Phi_{pp}(k_3, \omega; X_0) = \int_{-\infty}^{\infty} \Phi_{pp}(\zeta, \omega; X_0) e^{-jk_3\zeta}\, d\zeta \quad . \quad (7)$$

Again, the inhomogeneity of flow in the streamwise direction is considered. The homogeneity in the spanwise direction was verified by calculating the above statistics with different values of Z_0, which made no significant differences.

Figure 14 illustrates the spanwise coherence measured at $X_0/H = 2.0$ and $X_0/H = 8.0$. At $X_0/H = 2.0$, the coherence maintains values close to unity up to large distances in a wide frequency band centered at $fH/U_0 \sim 0.068$. At this initial stage of shear layer, the flow is virtually two-dimensional, and highly correlated across several step heights in the spanwise direction. In the downstream direction, the three-dimensionality starts to develop. This is reflected in Fig. 14b, where the coherence is reduced except for the frequency of large-scale vortices at $X_0/H = 8.0$. Note that the vortical structure maintains a considerable amount of spanwise coherence. These results in the spanwise direction again exemplify a unique feature of large-scale vortical characteristics of the pressure field.
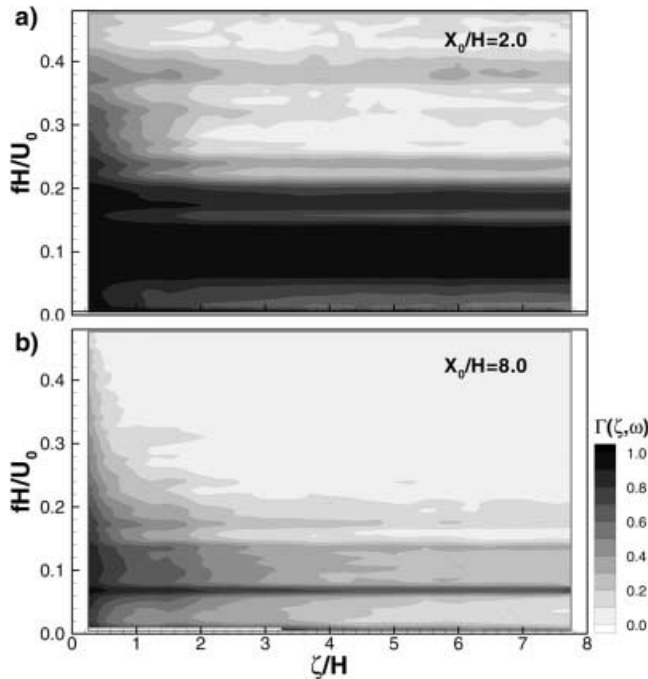
Fig. 14a, b. Contour plots of spanwise coherence at
a $X_0/H = 2.0$; **b** $X_0/H = 8.0$

Fig. 15a, b. Spanwise wavenumber–frequency spectra at
a $X_0/H = 4.0$; **b** $X_0/H = 10.0$

The spanwise wavenumber–frequency spectra obtained at $X_0/H = 4.0$ and $X_0/H = 10.0$ are presented in Fig. 15. Most energy is concentrated along the $k_3 = 0$ axis, which means a stationary two-dimensional mode. In addition, these spectra show nearly complete symmetry with respect to the k_3 coordinate. This can be regarded as another evidence of the spanwise homogeneity.

4
Conclusions

Statistical properties of the surface pressure fluctuations have been investigated experimentally for separated and reattaching flows over a backward-facing step with $\mathrm{Re}_H = 33,000$. Multi-point measurements with an array of microphones in the streamwise and spanwise directions provided a comprehensive data set of the spatiotemporal statistics of wall pressure fluctuations. One-point statistics, such as the streamwise distributions of rms pressure and autospectra, were shown to be generally consistent with other studies; the rms pressure attains a maximum slightly upstream of the reattachment point and the autospectra shows a peak from large-scale vortices. The fall-off rate approaches asymptotically the $-7/3$ power in high frequencies. The streamwise coherence measured at various locations attained local maxima at particular locations in the (ξ, ω) space. This behavior is in contrast to the Corcos model, where the coherence decays monotonically. These maxima moved with the reference point X_0, which is evidence of transverse spread of the separated shear layer along the streamwise direction. It was found that the spatial character of pressure fluctuations is classified into the coherent mode from large scale vortices and the decaying mode in high frequencies. The convection velocities are positive and converge to a value of 0.6 U_0 at high
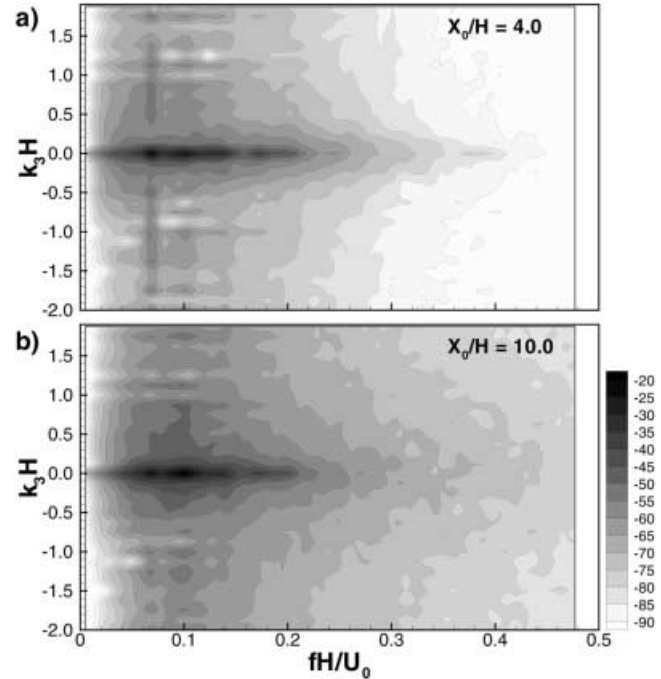
frequencies. This is consistent with the concept of over-riding-shear layer-generated pressure. The streamwise wavenumber–frequency spectra are indicative of the convective ridges with convection velocity of 0.6 U_0. The coherence and the wavenumber spectra in the spanwise direction demonstrate a unique feature of large-scale vortical characteristics of the pressure field. In addition to the orderly spatial structure, the streamwise wavenumber spectra suggest a modulation process of vortical structures by the flapping motion.

References

Adams EW; Johnston JP (1988) Flow structure in the near-wall zone of a turbulent separated flow. AIAA J 26: 932–939

Bendat JS; Piersol AG (1991) Random Data: Analysis and Measurement Procedure, 2nd Ed. John Wiley & Sons

Brederode V; Bradshaw P (1978) Influence of the side walls on the turbulent center-plane boundary-layer in a squareduct. J Fluid Eng 100: 91–96

Chang PA; Piomelli U; Blake WK (1999) Relationship between wall pressure and velocity-field sources. Phys Fluids 11: 3434–3448

Cherry NJ; Hillier R; Latour MEMP (1984) Unsteady measurements in a separated and reattaching flow. J Fluid Mech 144: 13–46

Choi H; Moin P (1990) On the space-time characteristics of wall-pressure fluctuations. Phys Fluids A 2: 1450–1460

Corcos GM (1964) The structure of the turbulent pressure field in boundary-layer flows. J Fluid Mech 18: 353–378

Chun KB; Sung HJ (1996) Control of turbulent separated flow over a backward-facing step. Exp Fluids 21: 417–426

Devenport WJ; Sutton EP (1991) Near-wall behavior of separated and reattaching flows. AIAA J 29: 25–31

Dhanak MR; Dowling AP; Si C (1997) Coherent vortex model for surface pressure fluctuations induced by the wall region of a turbulent boundary layer. Phys Fluids 9: 2716–2731

Driver DM; Seegmiller HL; Marvin JG (1987) Time-dependent behavior of a reattaching shear layer. AIAA J 25: 914–919

Eaton JK (1980) Turbulent flow reattachment: an experimental study of the flow and structure behind a backward-facing step. Doctoral Thesis, Stanford Univ

Eaton JK; Johnston JP (1981) A review of research on subsonic turbulent flow reattachment. AIAA J 19: 1093–1100

Farabee TM; Casarella MJ (1986) Measurements of fluctuating wall pressure for separated/reattached boundary layer flows. J Vibration, Acoustics, Stress and Reliability in Design 108: 301–307

Farabee TM; Casarella MJ (1991) Spectral features of wall pressure fluctuations beneath turbulent boundary layers. Phys Fluids A 3: 2410–2420

George WK; Beuther PD; Arndt RG (1984) Pressure spectra in turbulent free shear flows. J Fluid Mech 148: 155–191

Govinda Ram HS; Arakeri VH (1990) Studies on unsteady pressure fields in the region of separating and reattaching flows. J Fluids Eng 112: 402–408

Heenan AF; Morrison JF (1998) Passive control of pressure fluctuations generated by separated flow. AIAA J 36: 1014–1022

Kiya M; Sasaki K (1983) Structure of a turbulent separation bubble. J Fluid Mech 137: 83–113

Kiya M; Sasaki K (1985) Structure of large-scale vortices and unsteady reverse flow in the reattaching zone of a turbulent separation bubble. J Fluid Mech 154: 463–491

Le H; Moin P (1994) Direct numerical simulation of turbulent flow over a backward facing step. Department of Mech Eng, Stanford Univ., Report no. TF-58

Lee I; Sung HJ (1999) Development of an array of pressure sensors with PVDF film. Exp Fluids 26: 27–35

Mabey DG (1972) Analysis and correlation of data on pressure fluctuations in separated flow. J Aircraft 9: 642–645

Panton RL; Robert G (1994) The wavenumber–phase velocity representation for the turbulent wall-pressure spectrum. J Fluids Eng 116: 477–483

Schewe G (1983) On the structure and resolution of wall-pressure fluctuations associated with turbulent boundary-layer flow. J Fluid Mech 134: 311–328